

PAPER • OPEN ACCESS

Microstructural evolution in multiseeded YBCO bulk samples grown by the TSMG process

To cite this article: A Goodfellow *et al* 2016 *Supercond. Sci. Technol.* **29** 115005

View the [article online](#) for updates and enhancements.

Related content

- [Microstructure and trapped field of YBCO bulk single-grain superconductors prepared by interior seeding](#)
M Radusovska, P Diko, S Piovarci et al.
- [Growth-related microstructure of melt-grown REBa₂Cu₃O_y](#)
Pavel Diko
- [Growth related microstructure of Bridgman grown YBa₂Cu₃O₇/Y₂BaCuO₅ single-grain bars](#)
P Diko, K Zmorayova, E Mendoza et al.



can
superconductors

www.can-superconductors.com

HTS PARTS AND MATERIALS

Single and Multi-domain YBCO Bulk
REBCO Sputtering Targets
REBCO Powders and Granulates
BSCCO Current Leads, Magnetic Shields
Superconductivity Demonstration Kits

Microstructural evolution in multiseeded YBCO bulk samples grown by the TSMG process

A Goodfellow¹, Y-H Shi², J H Durrell², A R Dennis², D A Cardwell²,
C R M Grovenor¹ and S C Speller¹

¹Department of Materials, University of Oxford, UK

²Department of Engineering, University of Cambridge, UK

E-mail: susannah.speller@materials.ox.ac.uk

Received 29 July 2016, revised 7 September 2016

Accepted for publication 28 September 2016

Published 17 October 2016



CrossMark

Abstract

Superconducting single-grain YBCO bulk samples with the ability to trap high magnetic fields can be grown using the top-seeded melt-growth process. Multiseeding techniques have the potential to enable larger diameter bulks to be grown, but the performance of these materials is not yet comparable to the single-seeded bulks. Here we carry out detailed three-dimensional microstructural characterisation on a multiseeded sample grown with the seeds aligned in the 0°–0° geometry using high resolution microanalysis techniques. Chemical and structural variations have been correlated with the trapped field distribution in three separate slices of the sample. The top slice of the sample shows four peaks in trapped field, indicating that the current flows in four separate loops rather than in one large loop within the sample. This has been explained by the build-up in insulating Y-211 particles where the growth fronts from the two seeds meet, forming a barrier to current flow, as well as the low Y-211 content (and hence low J_c) of the large c -axis growth sector.

Keywords: YBCO, bulk, microstructure

(Some figures may appear in colour only in the online journal)

1. Introduction

The extraordinary ability of single grain bulk (RE)BaCuO (RE = rare Earth element) high temperature superconductors (HTS) to trap magnetic fields over 17 T at 26 K [1] leads to their potential application in practical devices including stable levitation [2] and flywheel energy storage devices using superconducting bearings [3, 4]. The top-seeded melt growth (TSMG) technique has been developed to grow single-grain (RE)BaCuO bulks with high critical current density (J_c), eliminating high-angle grain boundaries that act as weak links in HTS materials by ensuring nucleation occurs epitaxially

from the top of the sample at the seed crystal [5, 6]. The bulk crystal grows from the seed in five growth sectors; 4 a -axis growth sectors (a -GS) grow laterally outwards from the seed crystal in the a -axis direction and a c -axis growth sector (c -GS) extends downwards from directly beneath the seed, spreading out laterally in a square pyramid shape as it grows.

Since, according to the Bean model, the trapped field in bulk superconductors increases with increasing sample size, it is desirable to grow larger diameter single-grain samples. However in the TSMG process, slow growth rates are required to control the nucleation of the bulk and allow the peritectic formation of the superconducting (RE)Ba₂Cu₃O₇ phase, limiting the practical sample size that can be fabricated from a single nucleation point [7, 8]. Multiseeding is one method that has been used to grow larger samples and reduce processing time by using two or more seed crystals distributed



Original content from this work may be used under the terms of the Creative Commons Attribution 3.0 licence. Any further distribution of this work must maintain attribution to the author(s) and the title of the work, journal citation and DOI.

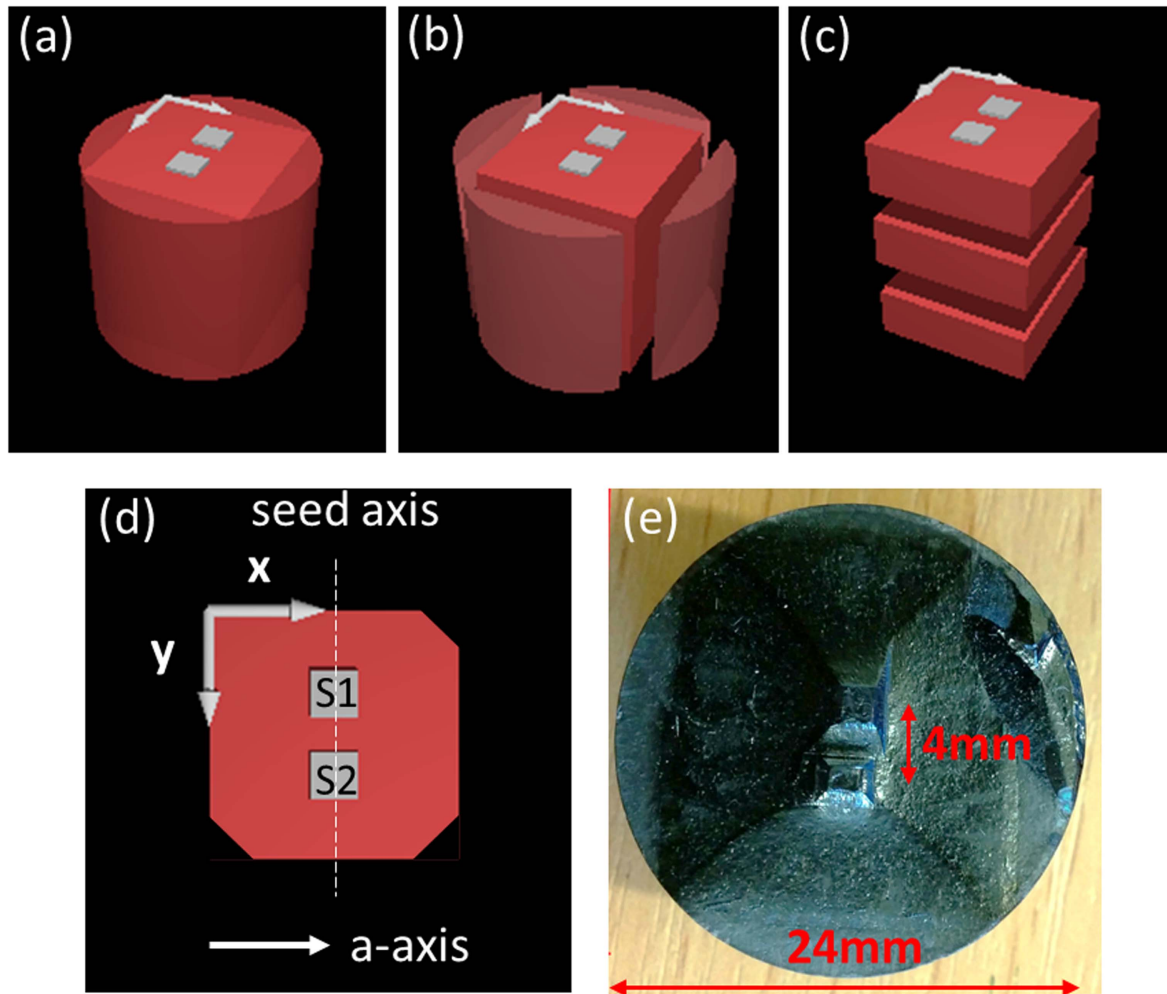


Figure 1. (a)–(c) Schematic diagrams showing how the bulk sample was sectioned for microscopy. (d) Schematic diagram of the top surface of the top section. (e) Photograph of the bulk sample before sectioning.

over the top surface to enable simultaneous nucleation from different sites [9–11]. A variety of seed arrangements have been studied, generally exhibiting rather inconsistent trapped field values attributed the presence of a grain boundary or residual liquid phase where the growth fronts meet [9, 10, 12, 13]. Bridge seeds have been used to successfully eliminate the formation of a high angle grain boundary where the growth fronts meet [14]. It has also been observed that samples grown from bridge seeds oriented in the 45° – 45° have improved trapped field performance compared to samples grown from bridge seeds in the 0° – 0° geometry [15]. It has been suggested that this arises because impurity phases pushed ahead of the growth fronts are trapped in the centre of the sample where the growth fronts meet head on in the 0° – 0° case, but are pushed outwards to the edges of the sample when the seeds are aligned in the 45° – 45° configuration [11]. Here we present a detailed examination of the microstructural development of a 0° – 0° multi-seeded bulk YBaCuO sample and compare the microstructure with trapped field for the same sample to enable the origin of the poor performance of these multiseeded bulks to be confirmed.

2. Experimental methods

A multiseeded sample has been grown by a modified TSMG process using a ‘bridge seed’ aligned in the so-called 0° – 0° geometry following the procedure described in detail in Shi *et al* [11]. The precursor powders were mixed in a composition ratio of 70 wt% Y-123 + 30 wt% Y-211 + 1 wt% CeO₂ and pressed into pellets 32 mm in diameter and 15 mm in height prior to melt-processing. The samples were heated initially to 1065 °C held for 1 h, and cooled at a rate of 75 °C h^{−1} to 1018 °C. Heterogeneous growth was then achieved by cooling the samples slowly and continuously to 1002 °C at a rate of 0.4 °C h^{−1} and then to 982 °C at 0.3 °C h^{−1}. Finally, the samples were cooled to room temperature at a rate of around 100 °C h^{−1}. To investigate the microstructural development, the cylindrical bulk sample was prepared by removing the curved edges and sectioning perpendicular to the *c*-axis into three slices of similar thickness using a slow diamond saw (see figure 1). Figure 1(e) shows the presence of a subsidiary Y-123 grain, the majority of which was removed during sectioning. After sectioning, the samples were annealed at 450 °C for seven days in flowing oxygen to drive

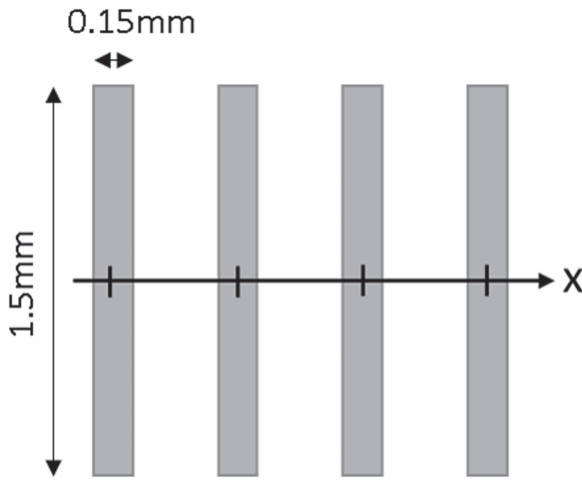


Figure 2. Schematic diagram showing how EDX 'linescans' were performed by measuring the average chemical composition of a series of regions (shown in grey) at discrete locations across the sample to obtain the spatial variation of $w_f(211)$.

the non-superconducting, tetragonal Y-123 phase to the superconducting orthorhombic phase.

A Zeiss Merlin scanning electron microscope (SEM), equipped with an Oxford Instruments 150 mm² Oxford Instruments X-max EDX detector, was used for BSE imaging and chemical composition analysis. The spatial distribution of the weight fraction of Y₂BaCuO₅ (Y-211) non-superconducting particles, added deliberately to improve flux pinning, has been estimated from EDX 'linescans' using the following procedure designed to allow the efficient mapping of large areas. The ratio of weight fractions of Y to Ba, averaged over both phases, was measured at each discrete location in the linescan by scanning the electron beam over regions about 1.5 mm by 0.15 mm in size (see figure 2). By assuming only two phases are present in the material, Y-123 of composition YBa₂Cu₃O₇ and Y-211 of composition Y₂BaCuO₅, the weight fraction of Y-211 ($w_f(211)$) at each location is related to the Y/Ba ratio by the equation:

$$w_f(211) = \frac{2R - A}{R(2 - M) + A(2M - 1)}, \quad (1)$$

where $R = \frac{\text{wt \% Y}}{\text{wt \% Ba}}$ measured by EDX, $A = \frac{A_r(\text{Y})}{A_r(\text{Ba})}$ is the ratio of the relative atomic masses of Y and Ba, and $M = \frac{m_r(123)}{m_r(211)}$ is the ratio of relative formula masses of Y-123 and Y-211.

Electron backscatter diffraction (EBSD) grain orientation mapping was carried out using a TSL system in a JEOL 6500F SEM and a JEOL 840A SEM. The Y-123 phase was indexed using a cubic unit cell to avoid mis-indexing as a result of the pseudosymmetry of Y-123 crystals [16, 17].

To assess the superconducting performance, each slice of the sample was field cooled to 77 K using liquid nitrogen with a field of 1.5 T applied perpendicular to its top surface. The applied field was then removed and the trapped field on the top surface of each sample measured using a rotating array of 20 Hall probes. The distance between the

sample surface and the Hall probes was estimated to be 0.7 mm.

3. Macroscopic overview of bulk structure and chemistry

Backscattered electron (BSE) imaging in a scanning electron microscope has been used to assess the structure of each slice of the sample at low magnification. The montage of images from the top slice (figure 3) shows a complex microstructure, with zones of columnar features extending laterally in the *a*-axis directions from the two seeds. The contrast observed in the BSE images originates from channelling of the BSEs along low symmetry crystallographic directions as they exit the sample rather than from chemical composition variations, as confirmed by EBSD (see inset of figure 3) and EDX mapping (not shown). These elongated subgrains, aligned along the local *a*-axis growth direction, and subgrain-free zones at the *a*-*a* growth sector boundaries (GSBs) are characteristic features of *a*-axis growth in REBCO bulks [18].

Directly beneath the position of each seed, no subgrain structures are observed in the BSE images, suggesting that growth in these regions is in the *c*-axis direction. In the central region between the two seeds, a small *a*-axis growth sector forms between the two *c*-GSs, with the subgrains aligned parallel to the seed axis (as defined in figure 1). Crystal growth in this region will be discussed in more detail in section 5. In addition, on the right hand edge of figure 3 the boundary with the subsidiary Y-123 grain mentioned previously can be observed.

Similar BSE low magnification imaging (not shown) reveals that in the middle slice there is a large subgrain-free zone corresponding to a single *c*-GS, with no sign of the central *a*-GS present in the top slice of the sample or the subsidiary Y-123 grain. The *c*-GS extends all the way to one of the edges of the sample, with the classic elongated subgrains visible in the *a*-GS regions around the other three edges. No columnar subgrain structures are visible anywhere on the bottom slice of the sample, suggesting that the *c*-GS extends across the entire width of the sample.

3.1. Macroscopic Y-211 particle distribution

EDX data showing the macroscopic variation in weight fraction of Y-211 particles ($w_f(211)$) across the multiseeded sample are presented in figure 4. The set of data taken parallel to the seed axis clearly shows that the Y-211 content drops abruptly to practically zero in the *c*-GS regions just below the seeds on the top slice of the sample. Within the *a*-GS regions the Y-211 content increases slightly from centre to edge of this sample. In the *a*-GS between the two seeds the $w_f(211)$ is about 0.3, but with a narrow region of much higher Y-211 content close to seed 2. This local build-up of Y-211 particles is discussed in more detail in section 5. The linescan perpendicular to the seeds passes across three different *a*-GSs in the top slice and also shows a slight increase in Y-211 content from the centre to the edge.

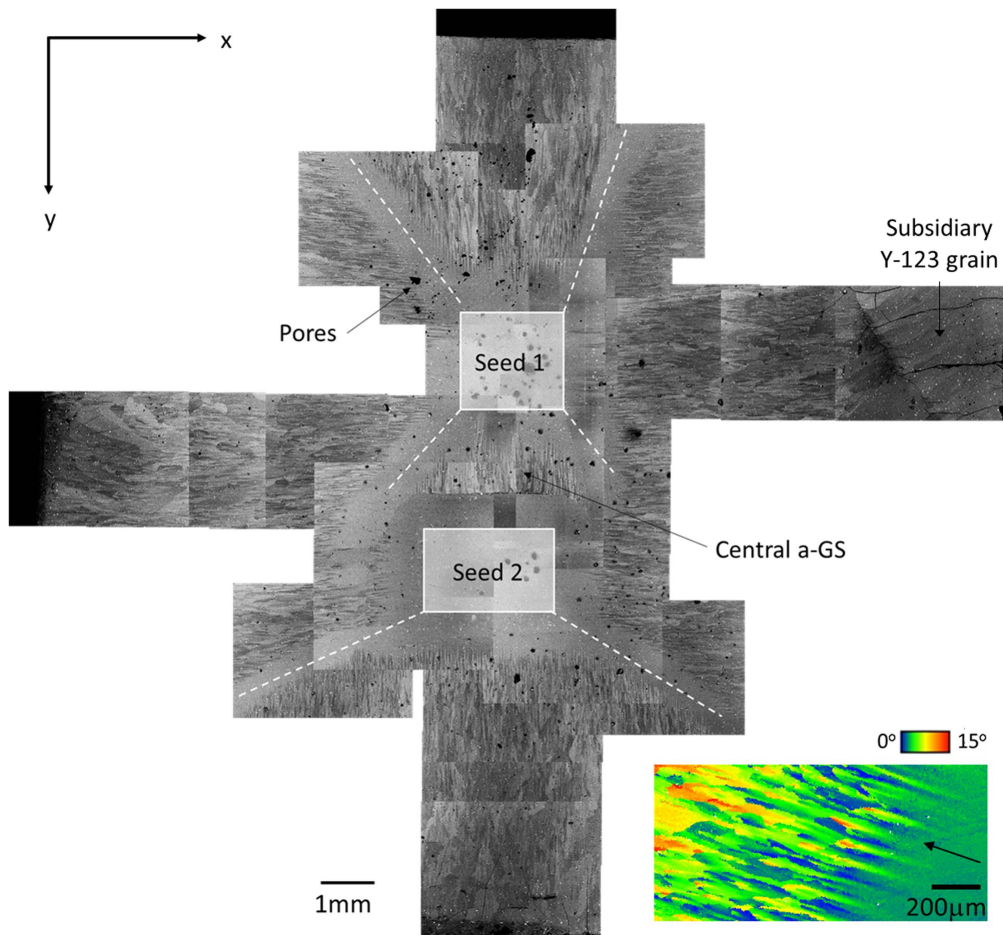


Figure 3. Montage of backscattered electron images from the top section of the multiseeded bulk sample with approximate positions of the two seeds marked, and the growth sector boundaries (GSB) indicated with white dashed lines. Inset: electron backscattered diffraction misorientation map showing development of *a*-axis subgrains in a standard TSMG sample, with growth direction labelled with an arrow.

The middle slice has a large central zone of low Y-211 content corresponding to the *c*-GS which extends right to the top edge of the sectioned sample (at $y = 0$). This low Y-211 content zone is about 10 mm wide in the direction perpendicular to the seed axis and at least 14 mm long along the seed axis. By comparison, in a standard sample grown from a single seed, the *c*-GS at a similar depth is much smaller at about 5 mm across [19, 20].

In the bottom slice of the multiseeded sample from the BSE images we expect *c*-axis growth across the entire sample. However there is considerable chemical inhomogeneity across the sample with low Y-211 content in the centre increasing dramatically towards the edges of the sample to $w_f(211)$ values above 0.4. Within the central region of the *c*-GS zones the Y-211 content increases slightly as growth progresses from the top to the bottom of the sample.

The inhomogeneous Y-211 particle distribution in standard TSMG samples grown from single seeds was explained by Endo *et al* [21] and subsequently by several other research groups using a particle pushing/trapping theory. In this theory, particles of Y-211 smaller than some critical radius (r^*) are pushed ahead of the solid Y-123 growth interface, whereas particles larger than r^* become trapped within the Y-123 grain. The value of r^* is related to interfacial energy

($\Delta\sigma_0$), melt viscosity (η) and growth rate (R) according to the following equations:

$$R \propto \frac{\Delta\sigma_0}{\eta r^*}, \quad (2)$$

$$\Delta\sigma_0 = \sigma_{sp} - \sigma_{tp} - \sigma_{sl}, \quad (3)$$

where σ_{sp} , σ_{tp} and σ_{sl} are the solid/particle, liquid/particle and solid/liquid interface energies respectively. The theory assumes that the Y-123 growth interface is planar and the Y-211 particles are spherical and inactive in the solidification process. However, since the peritectic solidification to form the Y-123 grain involves partial dissolution of the Y-211 particles, it is questionable whether the assumptions inherent in the particle pushing/trapping theory are valid in this case.

Qualitatively, the macrosegregation of Y-211 particles observed in the multiseeded sample is largely consistent with the particle pushing/trapping theory. As the growth proceeds the undercooling increases, resulting in an increase in growth rate and a decrease in critical radius for trapping. Consequently a larger proportion of the Y-211 particles will become trapped in the growing Y-123 grain, leading to an increase in the Y-211 content towards the edges of the sample. The σ_{sl} term in equation (3) is lower for *c*-axis growth than for *a*-

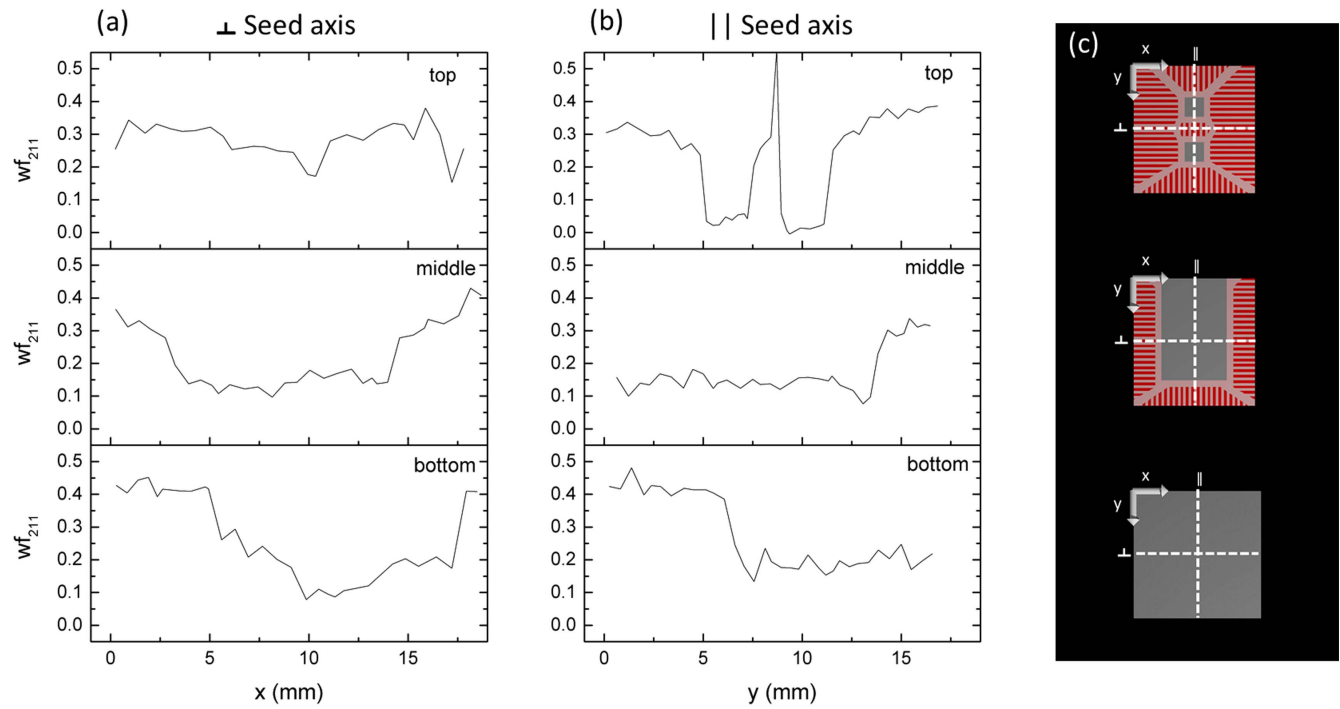


Figure 4. Variation in $w_f(211)$ in the top, middle and bottom sections of the sample in directions (a) perpendicular to the seed axis and (b) parallel to the seed axis. Schematics of the sample are given in (c), with the direction of the columnar subgrains in the a -GS shown in red/white stripes and the c -GS shown in grey.

axis growth as the (001) plane of Y-123 has a lower surface energy than the (100) plane [22]. This results in a higher value of $\Delta\sigma_0$ for c -axis growth, leading to a larger critical radius for a given growth rate (equation (2)) and hence lowering the fraction of Y-211 trapped in the c -GS regions relative to the a -GS. The weight fraction of Y-211 phase in the c -GS also increases from top to bottom as the undercooling increases. Within reason, the distribution of Y-211 can be controlled by changing the cooling rate during solidification. However, if the cooling rate is too high, multiple nucleation events will occur and the bulk will be polycrystalline, and if the cooling rate is too low, the liquid may drain out [20, 23].

4. Analysis of a -axis growth sector subgrain structures

Figure 5 shows EBSD orientation maps from an a -GS of the sample with typical elongated subgrains aligned along the a -axis growth direction. It can clearly be seen that in this region of the sample the grains are elongated along the y -direction—the local growth direction. The subgrain structures are only visible in the x and z misorientation maps, indicating that the subgrains are misoriented by rotations about the growth direction (y), producing tilt boundaries. The [001] pole figure shows a much greater spread in the data along the x -direction than the y -direction, confirming fibre texture about the growth direction (y) in this region of the bulk sample. Comparing the EBSD rocking curves, the full-width at half-maximum values for the misorientation about the y -axis is 3.6° compared to 1.5° about the x -axis.

To determine the three-dimensional morphology of the a -GS subgrains, vertical sections in the (a - c) plane have also been produced. Figure 6 shows an EBSD map taken from a vertical cross section near the top surface of a standard single-seeded TSMG sample, in an a -GS. The elongated subgrain structures visible confirm that the growth is columnar (rod-like) rather than having a plate-like morphology, as discussed by Diko [18]. In addition to the fine-scale columnar subgrain structures, there are additional subgrain boundaries visible (indicated by arrows in figure 6). These boundaries are separated by several hundred microns, and are not parallel to the a -axis.

The distinctive morphology of the a -GS subgrain structures can be used to elucidate the local growth direction. In addition to being elongated along the growth axis, the subgrain structures are observed to develop gradually, making it possible to ascertain along which direction the growth front had moved (figure 3 inset). EBSD has been used to investigate how the subgrain development relates to the increase in Y-211 content at the start of the a -GS (figure 7). By taking a series of high magnification EBSD maps, both phase (Y-123 or Y-211) and crystal orientation have been extracted from the EBSD patterns. The data clearly shows that the Y-211 particles start to appear 400–500 μm before the breakdown into columnar subgrains is visible. The large error bars on the Y-211 weight fraction data in areas 6 and 7 are a result of the high fraction of black pixels in the EBSD map where the diffraction pattern quality was too poor to index reliably.

The origin of the interface instability that leads to the development of columnar subgrains has been attributed by Diko [18] to the formation of dislocations in the growing Y-123 as Y-211 particles are trapped. This mechanism,

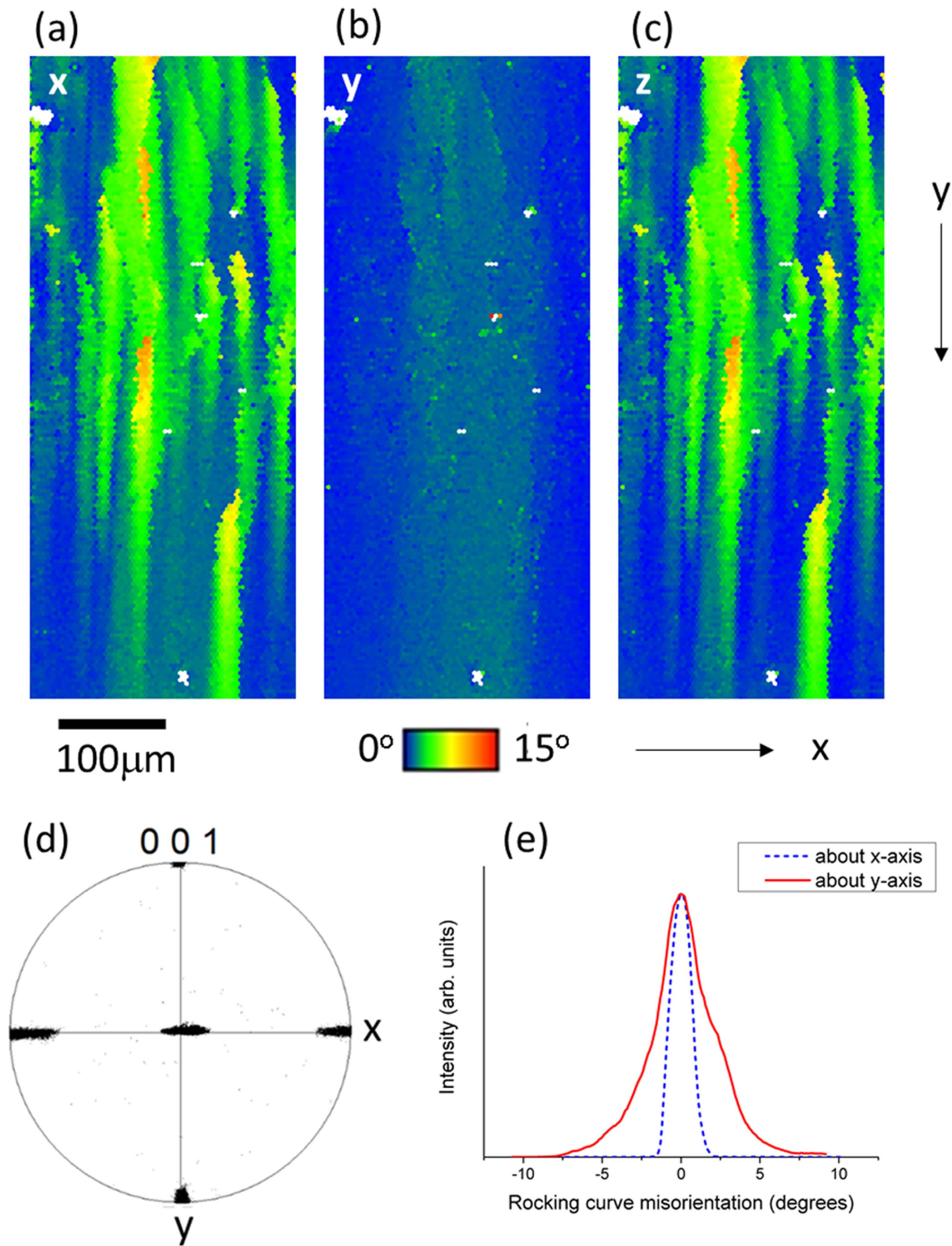


Figure 5. EBSD data from an *a*-GS with growth direction along the *y*-axis. EBSD maps showing (a), (b) *a*-axis misorientation to the in-plane *x*- and *y*-directions respectively, and (c) *c*-axis misorientation to the sample normal *z*-direction. (d) EBSD (001) pole figure constructed from the mapped area. (e) EBSD [100] rocking curves about the *x*- and *y*-directions.

described by Jackson [24], involves the rapid amalgamation of these dislocations at the growth interface where dislocation climb is easy, to form a series of low-angle grain boundaries that propagate with the growth interface in a dynamical polygonization process. Ogasawara *et al* [25] supported this interpretation based on their studies on SmBaCuO bulks in which

the subgrain structures are more pronounced. An alternative explanation involves the much more commonly observed phenomenon of constitutional supercooling which results in the breakdown of a planar interface into cellular structures. The separate cells can readily develop relative misorientations, and where they join together dislocations nucleate and rearrange

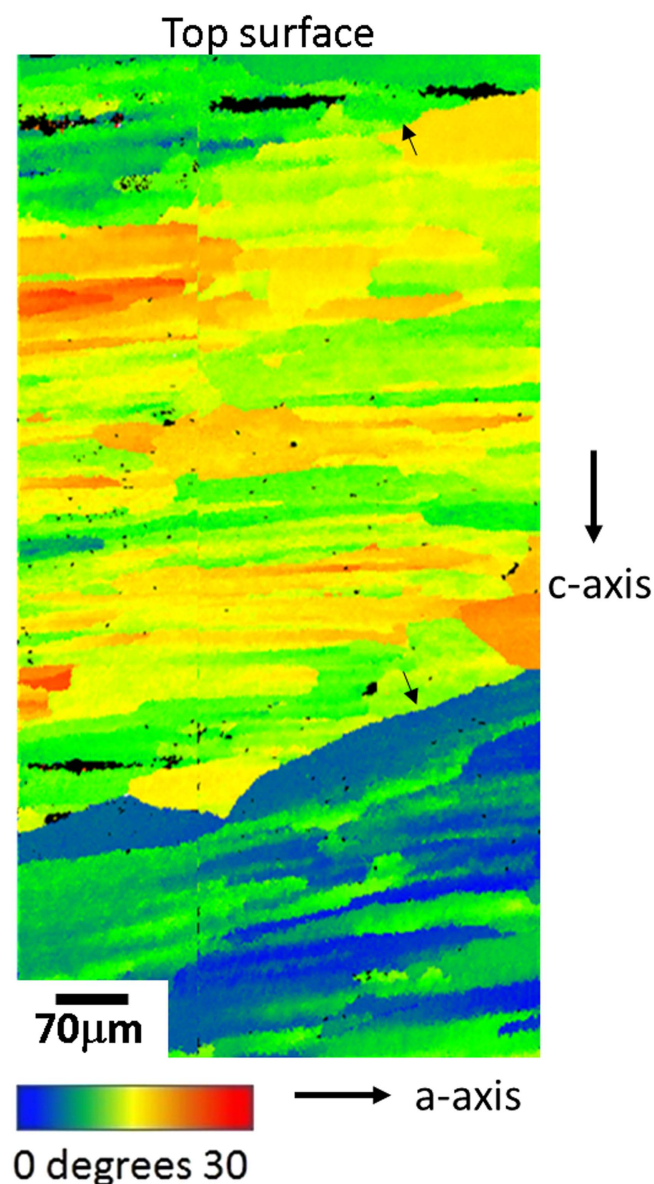


Figure 6. EBSD misorientation map on a vertical section of a standard single-seeded sample with the colour key showing the misorientation of the *a*-axis to the sample normal.

into low-angle subgrain boundaries [24]. Diko argues that the subgrain-free regions near the seed and the growth sector boundaries provide evidence for the dislocation-driven mechanism. However, this observation could also be explained by changes in the liquid chemistry ahead of the growth interface leading to an incubation time before the conditions for constitutional supercooling are met. It is not possible to distinguish between these two mechanisms from the final microstructures alone.

5. Microstructural evolution during growth

Figure 8 shows the region between the two seeds in the top slice of the multiseeded sample. The subgrain morphology clearly indicates that the growth front has moved in the *a*-axis

direction from seed 1 towards seed 2 in this region. The subgrain structures stop abruptly at a sharp interface where there is a narrow region where the EBSD patterns cannot be indexed as Y-123 (white pixels). No subgrain structures are present on the other side of this interface as the planar growth front from seed 2 has not advanced far enough to become unstable. EDX phase mapping shows that there is a build up of Y-211 particles at this interface where the growth fronts from the two seeds meet (figure 8(c)). This provides direct evidence that some of the Y-211 particles are pushed ahead of the growth interface. In addition, there are some larger BaCeO₃ particles present throughout the sample, indicating that at least some of the Ce₂O₃, added to prevent inhibit grain growth of the Y-211 particles, precipitates out rather than remaining in solid solution.

It is interesting to note that the *a*-axis growth fronts meet much closer to seed 2 than seed 1, presumably because nucleation occurred first at seed 1 in this particular sample, enabling the *a*-GS from seed 1 to grow almost all the way towards seed 2 before it meets the growth front approaching in the other direction from seed 2. This interface is too close to seed 2 for subgrain structures to have developed in this growth sector.

At the boundaries between adjacent *a*-GSs, a subgrain-free region forms as a result of there being a characteristic distance before breakdown of the planar growth interface occurs. EDX analysis across the GSB shows that there is no segregation of Y-211 particles to these boundary regions. This, coupled with the lack of crystallographic misalignment at the GSB, suggests that the growth fronts move away from the growth sector boundary rather than towards it, except possibly over rather short distances in the vicinity of the boundary.

As growth progresses downwards through the bulk sample, the two separate *c*-GSs spread laterally in a square pyramid shape, joining together to form a single, large *c*-GS. In the sample studied here, the growth is rather asymmetrical, with the large *c*-GS not located centrally in the bulk, as sketched in figure 4(c). This is probably a result of the grain growing from seed 1 more quickly than from seed 2, either because nucleation occurred first at seed 1 or because the *a*-axis growth rate was faster in this region. The Y-211 fraction is not distributed symmetrically in the bottom layer of the sample either, again highlighting the complex nature of the crystal growth.

6. Trapped field measurements

The trapped field distributions of each slice of the multiseeded sample have been measured, and the results shown in figure 9. The top slice shows four discrete peaks in trapped field, with the top right peak being somewhat weaker than the other three presumably owing to the presence of the subsidiary Y-123 grain observed in this region of the sample. This indicates that supercurrents mainly flow in four discrete loops within the four quadrants of the sample. Lack of current flow from the top half to the bottom half of the map is expected as the

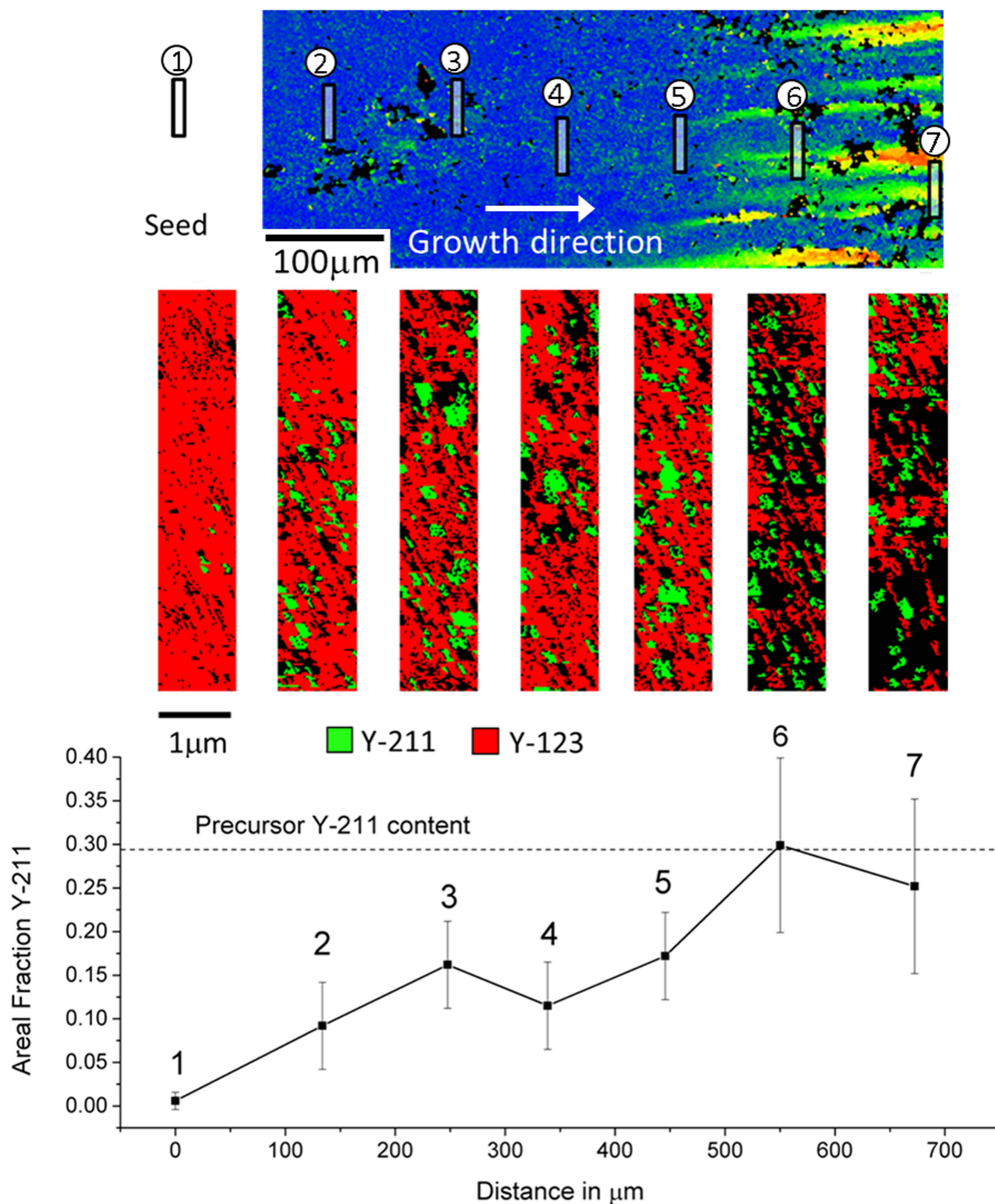


Figure 7. EBSD data comparing the start of breakdown of growth into columnar subgrains with the local fraction of Y-211 particles.

microstructural analysis in figure 8 has shown there is a barrier formed by a build-up of insulating Y-211 particles. More surprisingly, it is clear that it is not possible for large currents to flow from the left-hand side to the right-hand side

of this slice of the sample. This is likely to be a result of the extent of the *c*-axis growth sector lying beneath the surface, as shown schematically in figure 10. Since the concentration of Y-211 in the *c*-GS of this sample (shown in grey) is very low

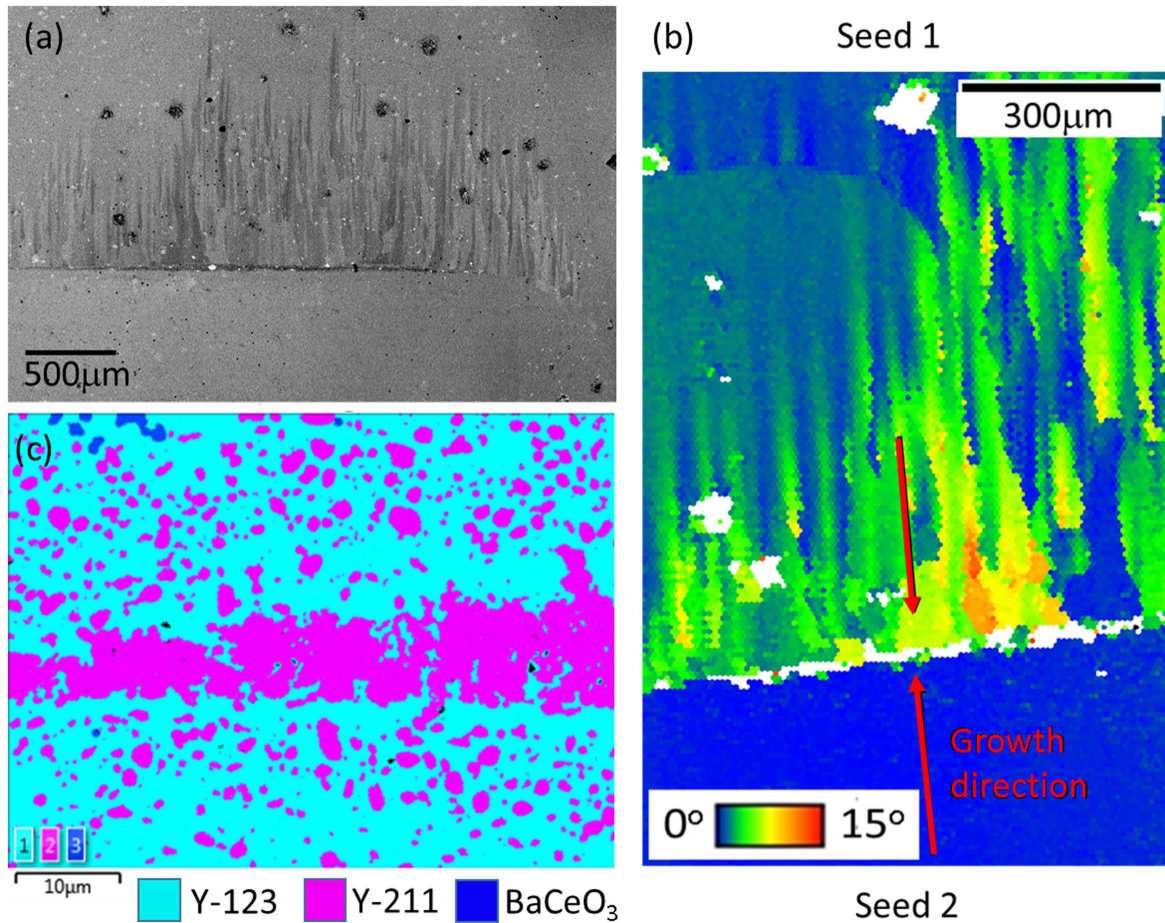


Figure 8. Columnar a -axis subgrains in central growth sector on top section imaged using (a) backscattered electrons and (b) EBSD orientation mapping. (c) Higher magnification EDX phase map showing a close-up of the interface where the growth fronts meet, with red arrows indicating local growth direction.

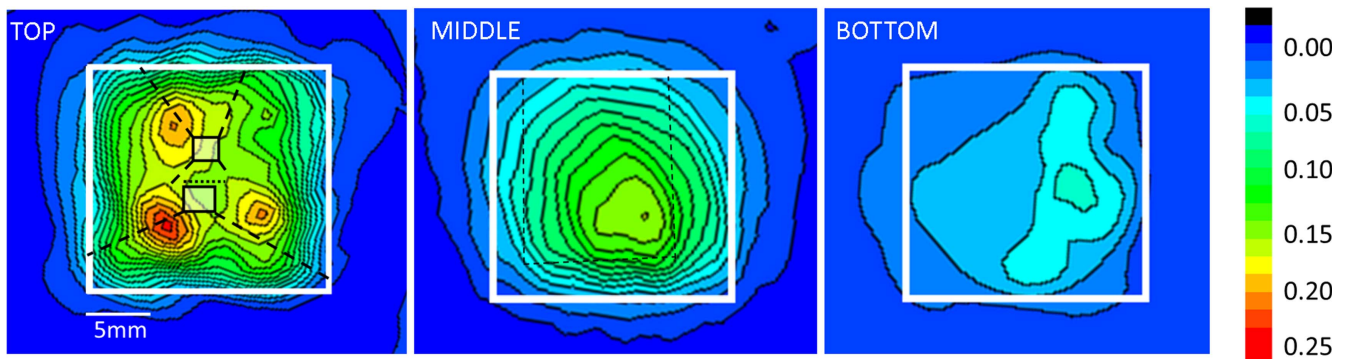


Figure 9. Trapped field distribution (in Tesla) measured xmm above the top surfaces of the top, middle and bottom slices of the multiseeded sample. The white box indicates the sample location, and the position of the main microstructural features are shown in black.

(see figure 4), the critical current density in this zone will be low, effectively splitting the left and right halves of the top slice of the sample as observed in the trapped field measurements. Alternatively, sub-surface defects that are not visible in the microscopy on the top surface, such as substantial microcracking, might be responsible for this behaviour.

The middle slice has a single peak in trapped field, with a much lower peak value of trapped field. In this slice, the c -GS

extends from the centre across the majority of the sample. Since this region has low Y-211 content, J_c values will be lower than in the a -GS of the top slice, leading to a lower peak trapped field value. The trapped field distribution shows a conventional single peaks, as J_c is more homogeneous in this slice and the current flow is not impeded by the barriers that were present in the top slice. The bottom slice of the sample has even poorer performance, with the trapped field being very low and rather inhomogeneously distributed. This

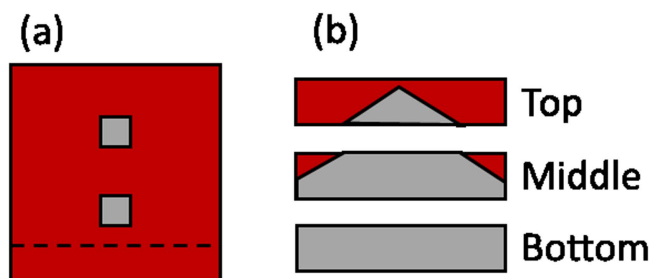


Figure 10. Schematic diagrams (a) of the top surface of the bulk with the dashed line indicating the position of the vertical section shown in (b). The *a*-GS regions are shown in red and the *c*-GS in grey.

is consistent with the large inhomogeneity in fraction of Y-211 in this slice of the sample seen in figure 4 and the expected breakdown of Y-123 growth near the bottom of the sample. It is worth noting that even the highest trapped field values measured in the top slice of the sample are rather lower than for previous samples [11]. This is likely to be a result of the smaller current loops and the very low Y-211 content in the *c*-GS of this particular sample.

7. Conclusions

This paper describes the first time that detailed three-dimensional microstructural characterisation, using a combination of high resolution EDX and EBSD techniques, has been correlated with the trapped magnetic field performance of slices of TSMG YBCO bulk. This analysis on a 0° – 0° multiseeded bulk has shown that there is a build-up of insulating Y-211 particles at the place where the *a*-axis growth sectors from the two separate seeds meet, producing a barrier to superconducting current flow, as hypothesised in previous work [11]. In addition, it has been shown that there is a very low Y-211 concentration in the *c*-axis growth sector. In combination with the Y-211 barrier, this has resulted in the top section of the bulk effectively behaving as four separate bulk magnets rather than one. In previous work, trapped field measurements from the entire thickness of a multiseeded sample with the seeds in the same geometry showed that the crystal effectively split into two portions rather than four. Here, by sectioning into slices, the detrimental effect of the low Y-211 content in the *c*-GS has become apparent, highlighting the importance of increasing the Y-211 content in the *c*-axis growth sector to optimise performance, particularly in multiseeded samples that have a much larger *c*-GS than standard single-seeded TSMG bulks. In addition, the subgrain structures in the *a*-axis growth sectors have been fully characterised, showing that the subgrains are misoriented with respect to each other by rotations about the growth direction. The morphology of the subgrains has also been used to assess the local growth direction, giving a comprehensive understanding of the crystal growth process.

Acknowledgments

We would like to acknowledge the Engineering and Physical Sciences Research Council (EPSRC grant EP/K02910X/1) for financial support. Data in support of this paper is accessible on the Oxford Research Archive (www.ora.ox.ac.uk) doi: 10.5287/bodleian:R59rr6pAk.

References

- [1] Durrell J H *et al* 2014 A trapped field of 17.6 T in melt-processed bulk Gd–Ba–Cu–O reinforced with shrink-fit steel *Supercond. Sci. Technol.* **27** 082001
- [2] Brandt E H 1990 Rigid levitation and suspension of high-temperature superconductors by magnets *J. Am. Phys.* **58** 43
- [3] Hull J 2000 Superconducting bearings *Supercond. Sci. Technol.* **27** R1
- [4] Strasik M, Hull J R, Mittleider J A, Gonder J F, Johnson P E, McCrarg K E and McIver C R 2010 An overview of boeing flywheel energy storage system with HTS bearings *Supercond. Sci. Technol.* **23** 034021
- [5] Sawano K, Morota M, Tanaka M, Sasaki T, Kimura K and Takebayashi S 1991 High magnetic flux trapping by melt-grown YBaCuO superconductors *Japan J. App. Phys.* **30** L1157
- [6] Cardwell D A 1998 Processing and properties of large grain (RE)BCO *Mater. Sci. Eng.* **B53** 1
- [7] Meng R L, Gao L, Gautier-Picard P, Ramirez D, Sun Y Y and Chu C W 1994 Growth and possible size limitation of quality single-grain YBa₂Cu₃O₇ *Physica C* **232** 337
- [8] Lo W, Cardwell D A, Dehurst C D and Dung S-L 1996 Fabrication of large grain YBCO by seeded peritectic solidification *J. Mater. Res.* **11** 786
- [9] Schatzle P, Krabbes G, Stover G, Fuchs D and ad Schlafer G 1999 Multi-seeded melt crystallisation of YBCO bulk materials for cryogenic applications *Supercond. Sci. Technol.* **2** 69
- [10] Kim C-J, Hong G-W and Oh H-J 2001 Multi-seeded melt growth processed YBCO superconductors *Physica C* **357** 635
- [11] Shi Y, Durrell J H, Dennis A R, Zhang Z, Zhai W, Babu N H and Cardwell D A 2013 A comparison of 0° – 0° and 45° – 45° bridge-seeded YBCO single grains *J. Am. Ceram. Soc.* **96** 1757
- [12] Kim C-J, Kim H-J, Jee Y-A, Hong G-W, Joo J-H, Han S-C, Han Y-H, Sung T-H and Kim S-J 2000 Effects of the seed distance on the characteristics of the (100)/(100) junctions of top-seeded melt growth processed YBCO superconductors using two seeds *Physica C* **336** 233
- [13] Delamare M P, Bringmann B, Jooss C, Walter H, Leenders A and Freyhardt H C 2002 Influence of seed distance on the microstructure and superconducting properties of grain boundaries in a multi-seeded melt growth monolith *Supercond. Sci. Technol.* **15** 16
- [14] Withnell T D, Babu N H, Iida K, Shi Y, Cardwell D A, Haindl S, Hernstberger F and Weber H W 2006 *Physica C* **382** 245–248
- [15] Ainslie M D, Zou J, Mochizuki H, Fujishiro H, Shi Y-H, Dennis A R and Cardwell D A 2015 Pulsed field magnetization of 00 and 4545 bridge-seeded YBaCuO bulk superconductors *Supercond. Sci. Technol.* **28** 125002
- [16] Weigand M, Speller S C, Hughes G M, Rutter N A, Lozano-Perez S, Grovenor C R M and Durrell J H 2010 Individual grain boundary properties and overall

- performance of metal-organic-deposited coated conductors *Phys. Rev. B* **81** 098017
- [17] Grossin D, Henrist C, Mathieu J-Ph, Meslin S, Harnois C, Noudam J-G, Cloots R and Chateigner D 2006 EBSD study on YBCO textured bulk samples: correlation between crystal growth and 'microtexture' *Supercond. Sci. Technol.* **19** 190
- [18] Diko P 2000 Growth-related microstructure of melt-grown (RE)Ba₂Cu₃O_y bulk superconductors *Supercond. Sci. Technol.* **13** 1202–13
- [19] Zhai W, Shi Y H, Durrell J H, Dennis A R, Rutter N A, Troughton S C, Speller S C and Cardwell D A 2013 The processing and properties of single grain Y–Ba–Cu–O fabricated from graded precursor powders *Supercond. Sci. Technol.* **26** 125021
- [20] Thoma M, Shi Y, Dennis T, Durrell J H and Cardwell D A 2015 Effect of Y-211 particle size on the growth of single grain Y–Ba–Cu–O bulk superconductors *J. Cryst. Growth* **412** 31
- [21] Endo A, Chouhan H S, Egi T and Shiohara Y 1996 Macrosegregation of Y₂Ba₁Cu₁O₅ particles in Y₁Ba₂Cu₃O_{7-δ} crystals grown by an undercooling method *J. Mater. Res.* **11** 795
- [22] Miletto Granozio F and Scotti di Uccio U 1997 Gibbs energy and growth habits of YBCO *J. Alloys Compd.* **251** 56
- [23] Zhai W, Shi Y, Durrell J H, Dennis A R and Cardwell D A 2014 The influence of Y-211 content on the growth rate and Y-211 distribution in Y–Ba–Cu–O single grains fabricated by top seeded melt growth *Cryst. Growth Des.* **14** 6367
- [24] Jackson K A 1971 *Solidification : Papers Presented at a Seminar of the American Society for Metals, 11–12 October 1969* (Materials Park, OH: American Society for Metals) pp 121
- [25] Ogasawara K, Sakai N and Murakami M 2001 Structure of subgrains in large single-grain RE–Ba–Cu–O (RE = Y, Sm, Nd) bulk superconductors *J. Cryst. Growth* **229** 358